

# Study some two loop contribution to muon MDM in the N-B-LSSM

Xing-Yu Han<sup>1,2,3</sup>, Jiao Ma<sup>1,2,3</sup>, Long Ruan<sup>1,2,3</sup>, Xi  
Wang<sup>1,2,3</sup>, Xing-Xing Dong<sup>1,2,3</sup>, Shu-Min Zhao<sup>1,2,3\*</sup>

<sup>1</sup> *Department of Physics, Hebei University, Baoding 071002, China*

<sup>2</sup> *Hebei Key Laboratory of High-precision Computation and  
Application of Quantum Field Theory, Baoding, 071002, China and*

<sup>3</sup> *Hebei Research Center of the Basic Discipline  
for Computational Physics, Baoding, 071002, China*

(Dated: July 2, 2024)

## Abstract

It is well known that the muon magnetic dipole moment (MDM) has close relation with the new physics (NP) in the development of the Standard Model (SM). Combined with the Fermilab National Accelerator Laboratory (FNAL) and the Brookhaven National Laboratory (BNL) E821 result, the departure from the SM prediction is about  $5.0 \sigma$ . We study the electroweak corrections from several type two-loop SUSY diagrams and the virtual SUSY particles include chargino, neutralino, scalar lepton and scalar neutrino. Based on the latest experimental constraints, we study the muon MDM under the next to the minimal supersymmetric extension of the SM with local B-L gauge symmetry (N-B-LSSM). The abundant numerical results verify that  $\tan \beta$ ,  $T_e$ ,  $M_L^2$ ,  $M_e^2$ ,  $M_{BB'}$  and  $M_{eij}^2$  play an important role in muon MDM.  $M_e^2$ ,  $\tan \beta$  and  $T_e$  are sensitive parameters to muon MDM. From the data obtained in all the figures of the numerical results, most of the values of  $a_\mu^{NBL}$  are in  $2\sigma$  interval, which can compensate the departure between the experiment data and the SM prediction.

PACS numbers:

Keywords: muon MDM, N-B-LSSM, Beyond Standard Model

---

\* zhaosm@hbu.edu.cn, hanxingyu223@163.com

## I. INTRODUCTION

In order to further study the properties and interactions of particles, the Standard Model (SM) theory of particle physics has been gradually established and developed by Glashow, Weinberg, Salam and others [1–4]. It unifies the three basic interactions of strong, weak, and electromagnetic. However, the SM still cannot explain some physical phenomena, such as the dark energy, the dark matter, the problem of gauge hierarchy and the absence of gravity, etc. Physicists have extended the SM based on the new symmetry of the combination of spatiotemporal symmetry and internal symmetry, resulting in the Minimal Supersymmetric Standard Model (MSSM) [5–7]. Although the MSSM can provide a dark matter candidate and alleviate hierarchy problem, it has not yet solved the  $\mu$  problem and neutrino mass problem. Based on the MSSM, next to the minimal supersymmetric extension of the SM with local B-L gauge symmetry (N-B-LSSM) extends the gauge symmetry group to  $SU(3)_C \times SU(2)_L \times U(1)_Y \times U(1)_{N-B-L}$ , where B represents the baryon number and L stands for the lepton number. N-B-LSSM has new superfields beyond MSSM, including three Higgs singlets  $\hat{\chi}_1, \hat{\chi}_2, \hat{S}$ .

It is well known that the muon magnetic dipole moment (MDM) has close relation with the new physics (NP) in the development of the SM. The SM contributions to muon MDM have the following parts: 1. the QED loop contributions [8–20]; 2. the electroweak contributions [21, 22]; 3. the hadronic vacuum polarization contributions [8, 11, 23]; 4. the hadronic light-by-light contributions [17–19]. The muon MDM is denoted by  $a_\mu \equiv (g_\mu - 2)/2$ . A new result on the muon MDM was reported by the E989 collaboration at Fermilab [24]:  $a_\mu^{FNAL} = 116592055(24) \times 10^{-11}(0.20\text{ppm})$ . The new averaged experiment value of muon anomaly is  $a_\mu^{exp} = 116592059(22) \times 10^{-11}(0.35\text{ppm})$ . Combining all available measurements, the SM prediction is more than  $5\sigma$  smaller than the updated world average [25]:  $\Delta a_\mu = a_\mu^{exp} - a_\mu^{SM} = 249(48) \times 10^{-11}$ .

The lattice Quantum Chromodynamics (QCD) method has been playing an increasingly important role in the precise calculation of non-perturbative low-energy hadron contributions to muon g-2, an important quantity in precision tests of the SM. In this context, the lattice QCD approach provides a first-principles framework to compute these contributions from the underlying theory of strong interactions. The lattice QCD method has the potential to reduce this deviation by providing more precise calculations of the hadronic vacuum

polarization (HVP) contribution, which is a major source of uncertainty in the SM prediction for muon  $g-2$ . The data  $\Delta a(HVP) = 105(59) \times 10^{-11}$  indicates that the deviation between theoretical predictions and experimental measurements will be greatly reduced. Due to the numerous experimental results, we refer to the central value of  $\Delta a(HVP)$  results, which is approximately  $85(56) \times 10^{-11}$  [8]. Considering the influence of QCD, it is possible to reduce the deviation between SM predictions and experiment data to 2.3 sigma. The one-loop correction of muon MDM has been well studied [26], but the study of two-loop correction is more complex and not deep enough. Using the effective Lagrangian method, the authors [27] calculate and derive the leading-logarithm two-loop contributions to the muon MDM. The authors research corrections to muon MDM from the two-loop rainbow diagrams and Barr-Zee diagrams with heavy fermion sub-loop in Refs.[28, 29]. The two-loop Barr-Zee type diagrams with fermion-sub-loop and scalar-sub-loop between vector boson and Higgs are studied in BLMSSM [30]. The muon MDM of two loop is also studied in the B-LSSM [31]. In this work, we study the electroweak corrections from several type two-loop SUSY diagrams and the virtual SUSY particles include chargino, neutralino, scalar lepton and scalar neutrino.

In Sec.II, we mainly introduce the N-B-LSSM including its superpotential, the general soft breaking terms, the mass matrices and couplings. In Sec.III, we give the analytical formulae of the one-loop and two-loop results of muon MDM in N-B-LSSM. The corresponding parameters and numerical analysis are shown in Sec.IV. The last section presents our conclusions. Finally, the Appendix shows some coupling vertices, mass matrixes and formulae that we need for this work.

## II. THE RELEVANT CONTENT OF N-B-LSSM

Using the local gauge group  $U(1)_{N-B-L}$ , we extend the MSSM to obtain the N-B-LSSM with the local gauge group  $SU(3)_C \times SU(2)_L \times U(1)_Y \times U(1)_{N-B-L}$ . N-B-LSSM has new superfields beyond MSSM, including three Higgs singlets  $\hat{\chi}_1, \hat{\chi}_2, \hat{S}$ .

In the chiral superfields,  $\hat{H}_u = \left( \hat{H}_u^+, \hat{H}_u^0 \right)$  and  $\hat{H}_d = \left( \hat{H}_d^0, \hat{H}_d^- \right)$  represent the MSSM-like doublet Higgs superfields.  $\hat{q}$  and  $\hat{l}$  are the doublets of quark and lepton.  $\hat{u}, \hat{d}, \hat{e}$  and  $\hat{\nu}$  are the singlet up-type quark, down-type quark, charged lepton and neutrino superfields,

TABLE I: The superfields in N-B-LSSM

Superfields	$U(1)_Y$	$SU(2)_L$	$SU(3)_C$	$U(1)_{N-B-L}$
$\hat{q}$	1/6	2	3	1/6
$\hat{l}$	-1/2	2	1	-1/2
$\hat{H}_d$	-1/2	2	1	0
$\hat{H}_u$	1/2	2	1	0
$\hat{d}$	1/3	1	$\bar{3}$	-1/6
$\hat{u}$	-2/3	1	$\bar{3}$	-1/6
$\hat{e}$	1	1	1	1/2
$\hat{\nu}$	0	1	1	1/2
$\hat{\chi}_1$	0	1	1	-1
$\hat{\chi}_2$	0	1	1	1
$\hat{S}$	0	1	1	0

respectively. We show the concrete forms of the two Higgs doublets and three Higgs singlets

$$\begin{aligned}
 H_d^0 &= \frac{1}{\sqrt{2}}\phi_d + \frac{1}{\sqrt{2}}v_d + i\frac{1}{\sqrt{2}}\sigma_d, \\
 H_u^0 &= \frac{1}{\sqrt{2}}\phi_u + \frac{1}{\sqrt{2}}v_u + i\frac{1}{\sqrt{2}}\sigma_u, \\
 \chi_1 &= \frac{1}{\sqrt{2}}\phi_1 + \frac{1}{\sqrt{2}}v_\eta + i\frac{1}{\sqrt{2}}\sigma_1, \\
 \chi_2 &= \frac{1}{\sqrt{2}}\phi_2 + \frac{1}{\sqrt{2}}v_{\bar{\eta}} + i\frac{1}{\sqrt{2}}\sigma_2, \\
 S &= \frac{1}{\sqrt{2}}\phi_S + \frac{1}{\sqrt{2}}v_S + i\frac{1}{\sqrt{2}}\sigma_S.
 \end{aligned} \tag{1}$$

The vacuum expectation values(VEVs) of the Higgs superfields  $H_u$ ,  $H_d$ ,  $\chi_1$ ,  $\chi_2$  and  $S$  are presented by  $v_u$ ,  $v_d$ ,  $v_\eta$ ,  $v_{\bar{\eta}}$  and  $v_S$  respectively. Two angles are defined as  $\tan\beta = v_u/v_d$  and  $\tan\beta_\eta = v_{\bar{\eta}}/v_\eta$ .

$$\begin{aligned}
 W &= -Y_d\hat{d}\hat{q}\hat{H}_d - Y_e\hat{e}\hat{l}\hat{H}_d - \lambda_2\hat{S}\hat{\chi}_1\hat{\chi}_2 + \lambda\hat{S}\hat{H}_u\hat{H}_d + \frac{\kappa}{3}\hat{S}\hat{S}\hat{S} + Y_u\hat{u}\hat{q}\hat{H}_u + Y_\chi\hat{\nu}\hat{\chi}_1\hat{\nu} \\
 &\quad + Y_\nu\hat{\nu}\hat{l}\hat{H}_u.
 \end{aligned} \tag{2}$$

In the superpotential for this model,  $Y_{u,d,e,\nu,\chi}$  are the Yukawa couplings.  $\lambda$ ,  $\lambda_2$  and  $\kappa$  are dimensionless couplings.  $\hat{\chi}_1$ ,  $\hat{\chi}_2$ ,  $\hat{S}$  are three Higgs singlets.

The soft SUSY breaking terms are

$$\begin{aligned}
\mathcal{L}_{soft} = & \mathcal{L}_{soft}^{MSSM} - \frac{T_\kappa}{3} S^3 + \epsilon_{ij} T_\lambda S H_d^i H_u^j + T_2 S \chi_1 \chi_2 \\
& - T_{\chi, ik} \chi_1 \tilde{\nu}_{R,i}^* \tilde{\nu}_{R,k}^* + \epsilon_{ij} T_\nu H_u^i \tilde{\nu}_{R,i}^* \tilde{e}_{L,j} - m_\eta^2 |\chi_1|^2 - m_{\tilde{\eta}}^2 |\chi_2|^2 \\
& - m_S^2 |S|^2 - m_{\nu, ij}^2 \tilde{\nu}_{R,i}^* \tilde{\nu}_{R,j} - \frac{1}{2} (2M_{BB'} \lambda_{\tilde{B}} \tilde{B}' + \delta_{ij} M_{BL} \tilde{B}'^2) + h.c. \quad .
\end{aligned} \tag{3}$$

$\mathcal{L}_{soft}^{MSSM}$  represent the soft breaking terms in the MSSM.  $T_\kappa$ ,  $T_\lambda$ ,  $T_2$ ,  $T_\chi$  and  $T_\nu$  are all trilinear coupling coefficients.

$U(1)_Y$  and  $U(1)_{N-B-L}$  have the gauge kinetic mixing effect, which can also be induced through RGEs even with zero value at  $M_{GUT}$ . The two Abelian gauge groups are unbroken, then the basis conversion can occur with the rotation matrix  $R$  ( $R^T R = 1$ ) [32–35].  $g_B$  is used to represent the gauge coupling constant of the  $U(1)_{N-B-L}$  group.  $g_{YB}$  is used to represent the mixing gauge coupling constant of  $U(1)_{N-B-L}$  group and  $U(1)_Y$  group. The covariant derivatives of this model can be written as

$$D_\mu = \partial_\mu - i \left( Y, B - L \right) \begin{pmatrix} g_Y, & g'_{YB} \\ g'_{BY}, & g'_{B-L} \end{pmatrix} \begin{pmatrix} A_\mu^Y \\ A_\mu^{BL} \end{pmatrix}, \tag{4}$$

where  $Y$  and  $B - L$  represent the hypercharge and  $B - L$  charge, respectively. The two Abelian gauge groups are unbroken, we can perform a change of basis

$$\begin{pmatrix} g_Y, & g'_{YB} \\ g'_{BY}, & g'_{B-L} \end{pmatrix} R^T = \begin{pmatrix} g_1, & g_{YB} \\ 0, & g_B \end{pmatrix}. \tag{5}$$

As a result, the  $U(1)$  gauge fields are redefined as

$$R \begin{pmatrix} A_\mu^Y \\ A_\mu^{BL} \end{pmatrix} = \begin{pmatrix} A_\mu^Y \\ A_\mu^{BL} \end{pmatrix}. \tag{6}$$

The mass matrix for neutralino in the basis  $(\lambda_{\tilde{B}}, \tilde{W}^0, \tilde{H}_d^0, \tilde{H}_u^0, \tilde{B}', \tilde{\chi}_1, \tilde{\chi}_2, S)$  is

$$m_{\chi^0} = \begin{pmatrix} M_1 & 0 & -\frac{1}{2}g_1v_d & \frac{1}{2}g_1v_u & M_{BB'} & 0 & 0 & 0 \\ 0 & M_2 & \frac{1}{2}g_2v_d & -\frac{1}{2}g_2v_u & 0 & 0 & 0 & 0 \\ -\frac{1}{2}g_1v_d & \frac{1}{2}g_2v_d & 0 & -\frac{1}{\sqrt{2}}\lambda v_S & -\frac{1}{2}g_{YB}v_d & 0 & 0 & -\frac{1}{\sqrt{2}}\lambda v_u \\ \frac{1}{2}g_1v_u & -\frac{1}{2}g_2v_u & -\frac{1}{\sqrt{2}}\lambda v_S & 0 & \frac{1}{2}g_{YB}v_u & 0 & 0 & -\frac{1}{\sqrt{2}}\lambda v_d \\ M_{BB'} & 0 & -\frac{1}{2}g_{YB}v_d & \frac{1}{2}g_{YB}v_u & M_{BL} & -g_Bv_\eta & g_Bv_{\bar{\eta}} & 0 \\ 0 & 0 & 0 & 0 & -g_Bv_\eta & 0 & -\frac{1}{\sqrt{2}}\lambda_2v_S & -\frac{1}{\sqrt{2}}\lambda_2v_{\bar{\eta}} \\ 0 & 0 & 0 & 0 & g_Bv_{\bar{\eta}} & -\frac{1}{\sqrt{2}}\lambda_2v_S & 0 & -\frac{1}{\sqrt{2}}\lambda_2v_\eta \\ 0 & 0 & -\frac{1}{\sqrt{2}}\lambda v_u & -\frac{1}{\sqrt{2}}\lambda v_d & 0 & -\frac{1}{\sqrt{2}}\lambda_2v_{\bar{\eta}} & -\frac{1}{\sqrt{2}}\lambda_2v_\eta & \sqrt{2}\kappa v_S \end{pmatrix}. \quad (7)$$

This matrix is diagonalized by the rotation matrix  $N$ ,

$$N^* m_{\chi^0} N^\dagger = m_{\chi^0}^{diag}. \quad (8)$$

One can find other mass matrixes in the Appendix A.

### III. ANALYTICAL FORMULA

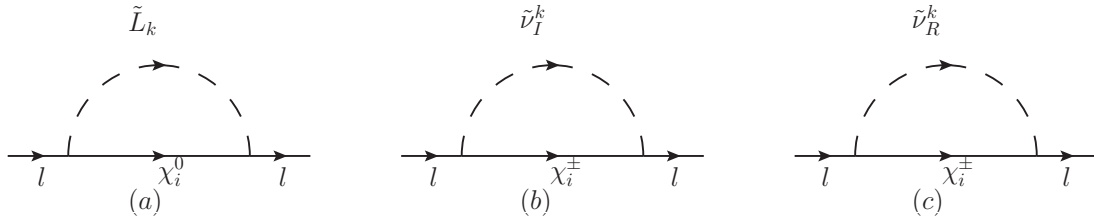


FIG. 1: The one-loop self-energy diagrams

With the effective Lagrangian method, the muon MDM can actually be expressed as

$$\mathcal{L}_{MDM} = \frac{e}{4m_l} a_l \bar{l} \sigma^{\mu\nu} l F_{\mu\nu}, \quad (9)$$

here,  $\sigma^{\mu\nu} = i[\gamma_\mu, \gamma_\nu]/2$ .  $m_l$  is the lepton mass,  $e$  and  $l$  denote the electric charge and the lepton fermion, and  $F_{\mu\nu}$  is the electromagnetic field strength.  $a_l$  is lepton MDM.

For the process  $l^I \rightarrow l^I + \gamma$ , the Feynman amplitude can be represented by some 6-dimensional operators. Since the higher-dimensional operators, such as the 8-dimensional

operators, are tiny, we ignore them. Their specific forms are

$$\begin{aligned}
\mathcal{O}_1^{L,R} &= \frac{1}{(4\pi)^2} \bar{l} (i\mathcal{D})^3 P_{L,R} l, & \mathcal{O}_2^{L,R} &= \frac{eQ_f}{(4\pi)^2} \overline{(i\mathcal{D}_\mu l)} \gamma^\mu F \cdot \sigma P_{L,R} l, \\
\mathcal{O}_3^{L,R} &= \frac{eQ_f}{(4\pi)^2} \bar{l} F \cdot \sigma \gamma^\mu P_{L,R} (i\mathcal{D}_\mu l), & \mathcal{O}_4^{L,R} &= \frac{eQ_f}{(4\pi)^2} \bar{l} (\partial^\mu F_{\mu\nu}) \gamma^\nu P_{L,R} l, \\
\mathcal{O}_5^{L,R} &= \frac{m_l}{(4\pi)^2} \bar{l} (i\mathcal{D})^2 P_{L,R} l, & \mathcal{O}_6^{L,R} &= \frac{eQ_f m_l}{(4\pi)^2} \bar{l} F \cdot \sigma P_{L,R} l,
\end{aligned} \tag{10}$$

with  $\mathcal{D}_\mu = \partial_\mu + ieA_\mu$  and  $P_{L,R} = \frac{1 \mp \gamma_5}{2}$ . The one loop contributions to the muon MDM are given by

$$a_\mu^{1L} = a_\mu^{1L}, \bar{L}\chi^0 + a_\mu^{1L}, \bar{\nu}^R \chi^\pm + a_\mu^{1L}, \bar{\nu}^I \chi^\pm. \tag{11}$$

The analytic form of  $a_\mu^{1L}, \bar{L}\chi^0, a_\mu^{1L}, \bar{\nu}^R \chi^\pm, a_\mu^{1L}, \bar{\nu}^I \chi^\pm$  are as follows

$$\begin{aligned}
a_\mu^{1L}, \bar{L}\chi^0 &= - \sum_{k=1}^6 \sum_{i=1}^8 \left[ \Re(A_L^* A_R) \sqrt{x_{\chi_i^0} x_\mu x_{\tilde{L}_k}} \frac{\partial^2 \mathcal{G}(x_{\chi_i^0}, x_{\tilde{L}_k})}{\partial x_{\tilde{L}_k}^2} \right. \\
&\quad \left. + \frac{1}{3} (|A_L|^2 + |A_R|^2) x_{\tilde{L}_k} x_\mu \frac{\partial \mathcal{G}_1(x_{\chi_i^0}, x_{\tilde{L}_k})}{\partial x_{\tilde{L}_k}} \right], \\
a_\mu^{1L}, \bar{\nu}^I \chi^\pm &= \sum_{i=1}^2 \sum_{k=1}^6 \left[ -2\Re(B_L^* B_R) \sqrt{x_{\chi_i^-} x_\mu} \mathcal{G}_1(x_{\tilde{\nu}_k^I}, x_{\chi_i^-}) \right. \\
&\quad \left. + \frac{1}{3} (|B_L|^2 + |B_R|^2) x_\mu x_{\chi_i^-} \frac{\partial \mathcal{G}_1(x_{\tilde{\nu}_k^I}, x_{\chi_i^-})}{\partial x_{\chi_i^-}} \right], \\
a_\mu^{1L}, \bar{\nu}^R \chi^\pm &= \sum_{i=1}^2 \sum_{k=1}^6 \left[ -2\Re(C_L^* C_R) \sqrt{x_{\chi_i^-} x_\mu} \mathcal{G}_1(x_{\tilde{\nu}_k^R}, x_{\chi_i^-}) \right. \\
&\quad \left. + \frac{1}{3} (|C_L|^2 + |C_R|^2) x_\mu x_{\chi_i^-} \frac{\partial \mathcal{G}_1(x_{\tilde{\nu}_k^R}, x_{\chi_i^-})}{\partial x_{\chi_i^-}} \right].
\end{aligned} \tag{12}$$

Here,  $x = \frac{m^2}{\Lambda^2}$ ,  $m$  is the particle mass. To save space in the text, the concrete forms of  $A_R, A_L, B_R, B_L, C_R, C_L$  can be found in the appendix A.  $\mathcal{G}(x, y)$  and  $\mathcal{G}_1(x, y)$  are defined as [36]

$$\mathcal{G}(x, y) = \frac{1}{16\pi^2} \left( \frac{x \ln x}{y-x} + \frac{y \ln y}{x-y} \right), \quad \mathcal{G}_1(x, y) = \left( \frac{\partial}{\partial y} + \frac{y}{2} \frac{\partial^2}{\partial y^2} \right) \mathcal{G}(x, y). \tag{13}$$

We ignore the contributions of neutral Higgs-lepton and charged Higgs-neutrino, which are suppressed by the square of the Higgs-lepton coupling  $\frac{m_\mu^2}{m_W^2} \sim 10^{-6}$ . We neglect the one-loop contribution of  $M_{Z'}$ -muon. Since the mass of the new vector boson  $M_{Z'}$  is greater than 5.1 TeV [37, 38], the one-loop contribution of  $M_{Z'}$ -muon is suppressed by the factor  $\frac{m_Z^2}{m_{Z'}^2} \sim 4 \times 10^{-4}$ .

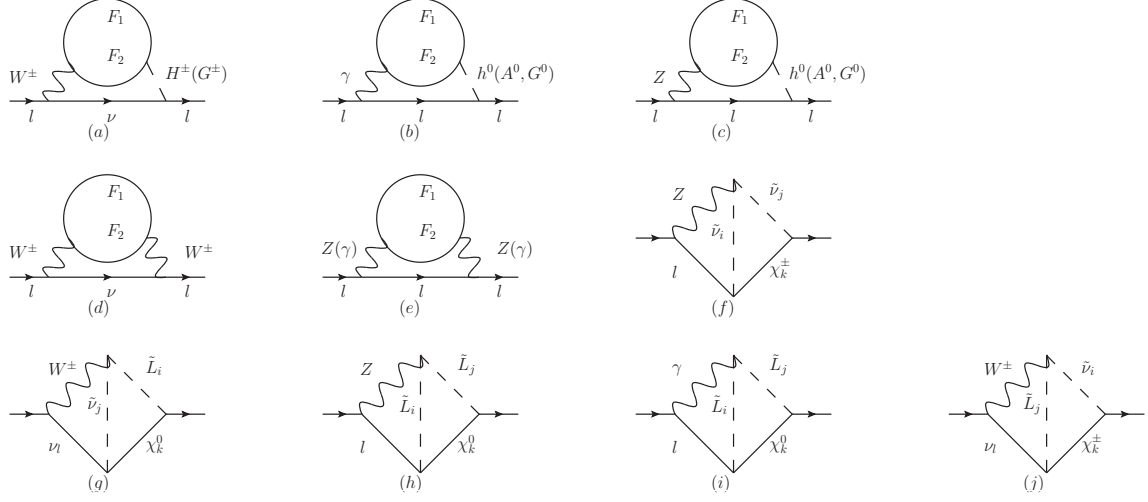


FIG. 2: The two-loop self-energy diagrams

The main contributions of two-loop graphs to muon MDM come from the following

1. The two-loop Barr-Zee type diagrams (Fig.2(a), Fig.2(b) and Fig.2(c)) with fermion sub-loop. In the work, the authors focus on their contributions to muon MDM[29]. On the supposition  $\chi^\pm \sim \chi^0 \sim M$ , we can obtain very concise results with the factor  $\frac{x_\mu}{x_M^{1/2} x_V^{1/2}} = \frac{m_\mu^2}{M m_V}$ .  $m_V$  represents the mass of heavy vector bosons  $m_Z \sim m_W \sim m_V$ . This analysis is in the mass eigenstate, and overall the rotation matrices to diagonalize the particle mass matrices should be taken into account. Then the order analysis in the mass insertion approximation is more appreciated, which shows the order as  $\frac{m_\mu^2}{M^2} \tan \beta$ .
2. Fig.2(d) and Fig.2(e) are the two-loop rainbow diagrams with fermion sub-loop and the vector bosons ( $\gamma$ ,  $Z$ ,  $W$ ). They have important contributions to muon MDM[39, 40].
3. The two-loop self-energy diagrams (Fig.2(f), ..., Fig.2(j)) belong to the diamond type. The diamond type diagrams in Ref.[41, 42] possess large factors. This type two-loop diagrams studied in this work contains five virtual particles including: one vector boson, two scalars and two fermions.

With the assumption  $m_{F_1} = m_{F_2} \gg m_W$ , the results [39] for the Fig.2 (a),(b),(c) can be simplified as

$$\begin{aligned}
a_\mu^{2L, WH} = & \frac{e C_{\bar{\mu} H \nu}^L}{512 \sqrt{2} \pi^4 s_W} \sum_{F_1 = \chi^\pm} \sum_{F_2 = \chi^0} \frac{x_\mu^{1/2}}{x_{F_1}^{1/2}} \left\{ \frac{199}{36} \Re(C_{H \bar{F}_1 F_2}^L C_{W \bar{F}_2 F_1}^L + H_{C \bar{F}_1 F_2}^R C_{W \bar{F}_2 F_1}^R) \right. \\
& \left. + \left[ \frac{13}{3} + 2(\ln x_{F_1} - \varrho_{1,1}(x_W, x_{H^\pm})) \right] \Re(C_{H \bar{F}_1 F_2}^L C_{W \bar{F}_2 F_1}^R + C_{H \bar{F}_1 F_2}^R C_{W \bar{F}_2 F_1}^L) \right\}
\end{aligned}$$

$$\begin{aligned}
& + \left[ \frac{4}{3} (\ln x_{F_1} - \varrho_{1,1}(x_W, x_{H^\pm})) - \frac{16}{9} \right] \Re(C_{H\bar{F}_1 F_2}^L C_{W\bar{F}_2 F_1}^L - C_{H\bar{F}_1 F_2}^R C_{W\bar{F}_2 F_1}^R) \\
& + \left[ \frac{2}{9} - \frac{8}{3} (\ln x_{F_1} - \varrho_{1,1}(x_W, x_{H^\pm})) \right] \Re(C_{H\bar{F}_1 F_2}^L C_{W\bar{F}_2 F_1}^R - C_{H\bar{F}_1 F_2}^R C_{W\bar{F}_2 F_1}^L) \Big\}, \quad (14)
\end{aligned}$$

$$\begin{aligned}
a_\mu^{2L, WG} &= \frac{e C_{\bar{\mu} G \nu}^L}{512 \sqrt{2} \pi^4 s_W} \sum_{F_1=\chi^\pm} \sum_{F_2=\chi^0} \frac{x_\mu^{1/2}}{x_{F_1}^{1/2}} \left\{ \frac{199}{36} \Re(C_{G\bar{F}_1 F_2}^L C_{W\bar{F}_2 F_1}^L + C_{G\bar{F}_1 F_2}^R C_{W\bar{F}_2 F_1}^R) \right. \\
& + \left[ \frac{7}{3} + 2(\ln x_{F_1} - \ln x_W) \right] \Re(C_{G\bar{F}_1 F_2}^L C_{W\bar{F}_2 F_1}^R + C_{G\bar{F}_1 F_2}^R C_{W\bar{F}_2 F_1}^L) \\
& + \left[ \frac{4}{3} (\ln x_{F_1} - \ln x_W) - \frac{28}{9} \right] \Re(C_{G\bar{F}_1 F_2}^L C_{W\bar{F}_2 F_1}^L - C_{G\bar{F}_1 F_2}^R C_{W\bar{F}_2 F_1}^R) \\
& \left. + \left[ \frac{26}{9} - \frac{8}{3} (\ln x_{F_1} - \ln x_W) \right] \Re(C_{G\bar{F}_1 F_2}^L C_{W\bar{F}_2 F_1}^R - C_{G\bar{F}_1 F_2}^R C_{W\bar{F}_2 F_1}^L) \right\}. \quad (15)
\end{aligned}$$

$$a_\mu^{2L, \gamma h^0} = \frac{e^2}{64 \sqrt{2} \pi^4} C_{h^0 \bar{\mu} \mu} \sum_{F_1=F_2=\chi^\pm} \frac{x_\mu^{1/2}}{x_{F_1}^{1/2}} \Re(C_{h^0 \bar{F}_1 F_2}^L) \left[ 1 + \ln \frac{x_{F_1}}{x_{h^0}} \right], \quad (16)$$

$$\begin{aligned}
a_\mu^{2L, Zh^0} &= \frac{\sqrt{2}}{512 \pi^4} \sum_{F_1=F_2=\chi^\pm, \chi^0} C_{h^0 \bar{\mu} \mu} \frac{x_\mu^{1/2}}{x_{F_1}^{1/2}} \left[ \varrho_{1,1}(x_Z, x_{h^0}) - \ln x_{F_1} - 1 \right] \times (C_{Z\bar{\mu} \mu}^L + C_{Z\bar{\mu} \mu}^R) \\
& \Re(C_{h^0 \bar{F}_1 F_2}^L C_{Z\bar{F}_2 F_1}^L + C_{h^0 \bar{F}_1 F_2}^R C_{Z\bar{F}_2 F_1}^R). \quad (17)
\end{aligned}$$

To save space in the text, the complete calculation process and the results of other two-loop diagrams can be found in our previous work [36]. The corrections to muon MDM from the studied two-loop diagrams are

$$\begin{aligned}
a_\mu^{2L} &= a_\mu^{2L, BZ} + a_\mu^{2L, RB} + a_\mu^{2L, DIA}, \\
a_\mu^{2L, BZ} &= a_\mu^{2L, WH} + a_\mu^{2L, WG} + a_\mu^{2L, \gamma h^0} + a_\mu^{2L, \gamma G_0} + a_\mu^{2L, \gamma A_0} \\
& \quad + a_\mu^{2L, Zh^0} + a_\mu^{2L, ZG_0} + a_\mu^{2L, ZA_0}, \\
a_\mu^{2L, RB} &= a_\mu^{2L, WW} + a_\mu^{2L, ZZ} + a_\mu^{2L, Z\gamma} + a_\mu^{2L, \gamma\gamma}, \\
a_\mu^{2L, DIA} &= a_\mu^{2L, Z\tilde{\nu}\chi^\pm} + a_\mu^{2L, Z\tilde{L}\chi^0} + a_\mu^{2L, \gamma\tilde{L}\chi^0} + a_\mu^{2L, W\tilde{L}\tilde{\nu}\chi^0} + a_\mu^{2L, W\tilde{L}\tilde{\nu}\chi^-}. \quad (18)
\end{aligned}$$

The concrete expressions can be found in Appendix A.

At two-loop level, including the one-loop results and two-loop results, the muon MDM is given by

$$a_\mu^{NBL} = a_\mu^{1L} + a_\mu^{2L}. \quad (19)$$

#### IV. NUMERICAL ANALYSIS

To take the numerical calculation, some restrictions should be taken into account.

1. The experimental value of  $\tan \beta_\eta$  should be less than 1.5 in order to meet the LHC experimental data [43].
2. The limitations from neutrino experimental data are taken into account [44].
3. We consider the experimental constraints from the lightest CP-even Higgs  $h^0$  mass is around 125.25 GeV [44, 45].
4. The  $Z'$  boson mass is larger than 5.1 TeV. The ratio between  $M_{Z'}$  and its gauge  $M_{Z'}/g_B \geq 6$  TeV [37, 38].
5. For particles that exceed the SM, the mass limits considered are: the slepton mass is greater than 700 GeV, the squark mass is maintained at the TeV order of magnitude, and the chargino mass is greater than 1100 GeV [44].

Considering these limitations, we adopt the following parameters:

$$\begin{aligned}
\kappa &= 0.1, & \tan \beta_\eta &= 0.9, & g_B &= 0.3, & g_{YB} &= 0.1, & v_S &= 4 \text{ TeV}, \\
\lambda &= 0.4, & M_1 &= 0.1 \text{ TeV}, & M_2 &= 1.2 \text{ TeV}, & \lambda_2 &= -0.25, \\
T_\lambda &= T_{\lambda_2} = 1 \text{ TeV}, & T_\kappa &= -2.5 \text{ TeV}, & M_{BL} &= 1 \text{ TeV}, & T_{uii} &= 1 \text{ TeV}, \\
Y_{\nu_{11}} &= 1.09285 \times 10^{-6}, & Y_{\nu_{22}} &= 1.4 \times 10^{-6}, & Y_{\nu_{33}} &= 1.35242 \times 10^{-6}, \\
Y_{\nu_{12}} &= 7.6042 \times 10^{-8}, & Y_{\nu_{13}} &= 4.51693 \times 10^{-8}, & Y_{\nu_{23}} &= 2.80323 \times 10^{-7}.
\end{aligned} \tag{20}$$

We generally take the values of new particle masses ( $M_{BB'}$ ,  $M_{BL}$ ) near the order of  $10^3$  GeV, which is around the energy scale of new physics.  $T_\lambda$  and  $T_2$  etc. are trilinear coupling coefficients, which are roughly in the order of magnitude of the mass, and can be varied up or down to the order of  $10^2 \sim 10^4$  GeV.  $M_L^2$ ,  $M_e^2$  are all of mass square dimension, and can be up to the order of  $10^6$  GeV<sup>2</sup>. The dimensionless parameters  $\lambda$  and  $\lambda_2$  etc. are generally taken as numbers less than 1.

We use the "top-down" method to derive the formulas of neutrino mass and mixing angle from the effective neutrino mass matrix. The specific derivation formulas can be found in the Appendix A.

To fit the data of neutrino physics, with the normal order supposition we take the parameters as

$$\begin{aligned}
\tan \beta &= 20, & \tan \beta_\eta &= 0.9, & v_{\bar{\eta}} &= 17000 \times \sin \theta_\eta \text{ GeV}, & Y_\chi &= 0.1, \\
Y_{\nu_{11}} &= 1.09285 \times 10^{-6}, & Y_{\nu_{22}} &= 1.4 \times 10^{-6}, & Y_{\nu_{33}} &= 1.35242 \times 10^{-6}, \\
Y_{\nu_{12}} &= 7.6042 \times 10^{-8}, & Y_{\nu_{13}} &= 4.51693 \times 10^{-8}, & Y_{\nu_{23}} &= 2.80323 \times 10^{-7}.
\end{aligned} \tag{21}$$

Then we obtain neutrino data in the following form, which can well satisfy the constraints from neutrino experiment

$$\begin{aligned}\sin^2(\theta_{12}) &= 0.307, & \sin^2(\theta_{23}) &= 0.547, & \sin^2(\theta_{13}) &= 0.022, \\ \Delta m_{\odot}^2 &= 7.53 \times 10^{-5} \text{ eV}^2, & |\Delta m_A^2| &= 2.437 \times 10^{-3} \text{ eV}^2.\end{aligned}\quad (22)$$

The three neutrino masses are at sub eV order as follows

$$m_{\nu_1} = 0.0221031 \text{ eV}, \quad m_{\nu_2} = 0.0237454 \text{ eV}, \quad m_{\nu_3} = 0.0540883 \text{ eV}. \quad (23)$$

In the following numerical analysis process, the parameters that need to be studied are:

$$\begin{aligned}\tan \beta, \quad T_{eii} = T_e, \quad M_{lii}^2 = M_l^2, \quad M_{eii}^2 = M_e^2, \\ M_{BB'}, \quad T_{eij} = T_{eji}, \quad M_{eij}^2 = M_{eji}^2, \quad (i = 1, 2, 3), \quad (i \neq j).\end{aligned}\quad (24)$$

In addition to the above parameters, non diagonal elements are defined as zero.

### A. The one-dimensional graphs

We use the simplified expression of  $\chi_{NBL}^2$  as

$$\chi_{NBL}^2 = e^{-\left(\frac{\Delta a_\mu - a_\mu^{NBL}}{\delta a_\mu}\right)^2}, \quad (25)$$

with  $\Delta a_\mu = 249 \times 10^{-11}$ ,  $\delta a_\mu = 48 \times 10^{-11}$ . This formula clearly indicates the deviation of  $a_\mu^{NBL}$  and  $\Delta a_\mu$ . When  $a_\mu^{NBL}$  approaches  $\Delta a_\mu$ ,  $\chi_{NBL}^2$  approaches 1.

The light gray and light orange regions in all figures represent the experimental limits of  $\Delta a_\mu$ , where the light gray region represents the  $1\sigma$  range of  $\Delta a_\mu$ , and the light orange region represents the  $2\sigma$  range of  $\Delta a_\mu$ .

With the parameters  $\tan \beta = 10$ ,  $T_{eii} = 3 \text{ TeV}$ ,  $M_{BB'} = 0.1 \text{ TeV}$ ,  $M_{eij}^2 = 0$  and  $T_{eij} = 0$  in Fig.3(a), we plot  $M_e^2$  versus  $a_\mu^{NBL}$  and  $\chi_{NBL}^2$ . The two lines are all decreasing functions as  $M_e^2$  turns large in the range of  $1.48 \text{ TeV}^2 < M_e^2 < 2.5 \text{ TeV}^2$ . When  $M_e^2$  is in the range of  $1.48 \text{ TeV}^2$  to  $1.7 \text{ TeV}^2$ ,  $a_\mu^{NBL}$  is in the  $1\sigma$  interval. When  $M_e^2$  is in the range of  $1.7 \text{ TeV}^2$  to  $2.5 \text{ TeV}^2$ ,  $a_\mu^{NBL}$  is in the  $2\sigma$  interval. The expression of  $\chi_{NBL}^2$  indicates that as the value of  $a_\mu^{NBL}$  deviates from  $\Delta a_\mu$ ,  $\chi_{NBL}^2$  becomes smaller. When  $a_\mu^{NBL}$  approaches  $\Delta a_\mu$ ,  $\chi_{NBL}^2$  approaches 1. The image meanings of  $\chi_{NBL}^2$  and  $a_\mu^{NBL}$  in the figure are consistent. We plot

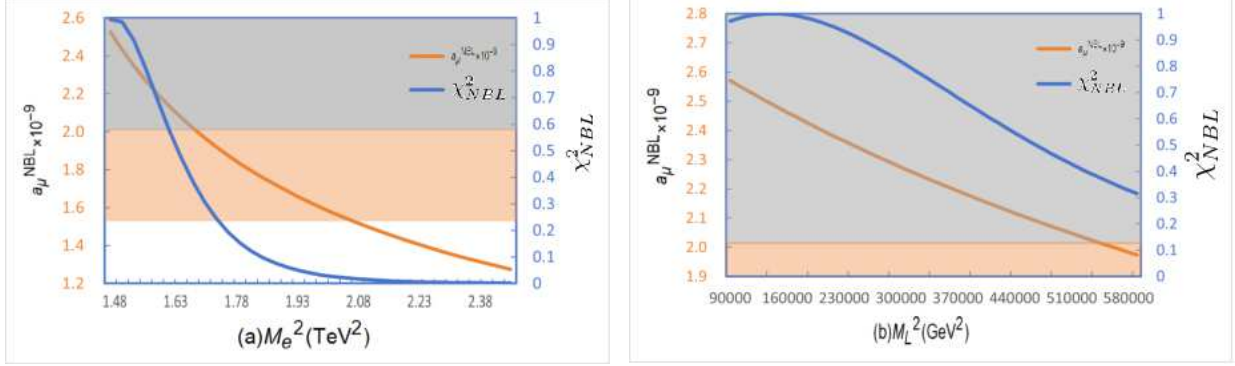


FIG. 3:  $a_\mu^{NBL}$  and  $\chi_{NBL}^2$  in  $M_e^2$  plane (a) and  $M_L^2$  plane (b).

$M_L^2$  versus  $a_\mu^{NBL}$  and  $\chi_{NBL}^2$  in the Fig.3(b).  $a_\mu^{NBL}$  and  $\chi_{NBL}^2$  show a downward trend with the increase of  $M_L^2$ .  $a_\mu^{NBL}$  is mostly in the range of  $1\sigma$ , and the trend of  $\chi_{NBL}^2$  is consistent with  $a_\mu^{NBL}$ .

$M_L^2$  is the parameter appearing in the mass matrices of the CP-odd sneutrino, the CP-even sneutrino, and the slepton.  $M_e^2$  just appears in the mass matrix of the slepton. The increase of  $M_e^2$  and  $M_L^2$  makes sneutrino and slepton heavy, which suppresses the contributions from the CP-odd sneutrino, the CP-even sneutrino, and the slepton. Thereby  $a_\mu^{NBL}$  decreases with the increase of  $M_e^2$  and  $M_L^2$ .

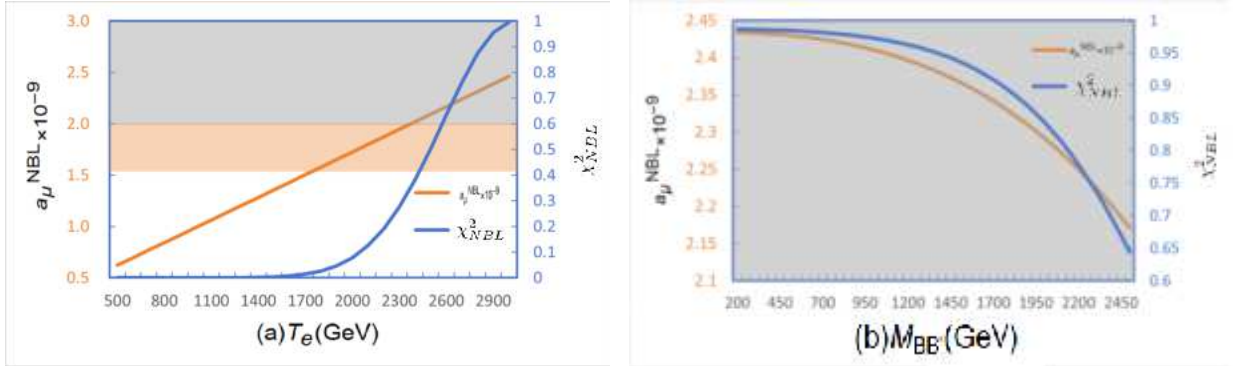


FIG. 4:  $a_\mu^{NBL}$  and  $\chi_{NBL}^2$  in  $T_e$  plane (a) and  $M_{BB'}$  plane (b).

We suppose  $\tan\beta = 10$ ,  $M_e^2 = 1.5 \text{ TeV}^2$ ,  $M_L^2 = 0.16 \text{ TeV}^2$ ,  $M_{eij}^2 = 0$ ,  $T_{eij} = 0$ . Similarly, we plot  $T_e$  versus  $a_\mu^{NBL}$  and  $\chi_{NBL}^2$  in the Fig.4(a). In this figure,  $a_\mu^{NBL}$  significantly increases with the growth of  $T_e$ . When  $T_e$  is greater than 1.7 TeV, it enters the  $2\sigma$  range, and when  $T_e$  is greater than 2.4 TeV, it enters the  $1\sigma$  range.  $\chi_{NBL}^2$  is also showing a growth trend. In

addition, we study the parameter  $M_{BB'}$  influences on  $a_\mu^{NBL}$  and  $\chi_{NBL}^2$  in Fig.4(b). When  $0.2 \text{ TeV} < M_{BB'} < 2.45 \text{ TeV}$ , both lines decrease with the increase of  $M_{BB'}$ , indicating that  $a_\mu^{NBL}$  is in the  $1\sigma$  region throughout the entire range.  $M_{BB'}$  is the mass of the two U(1) gauginos mixing, and appears as the non-diagonal element of the neutralino mass matrix. The increase in  $M_{BB'}$  has affected the neutralino mass matrix, leading to a downward trend in  $a_\mu^{NBL}$ , and the curve of  $\chi_{NBL}^2$  indicates that this effect is relatively strong.

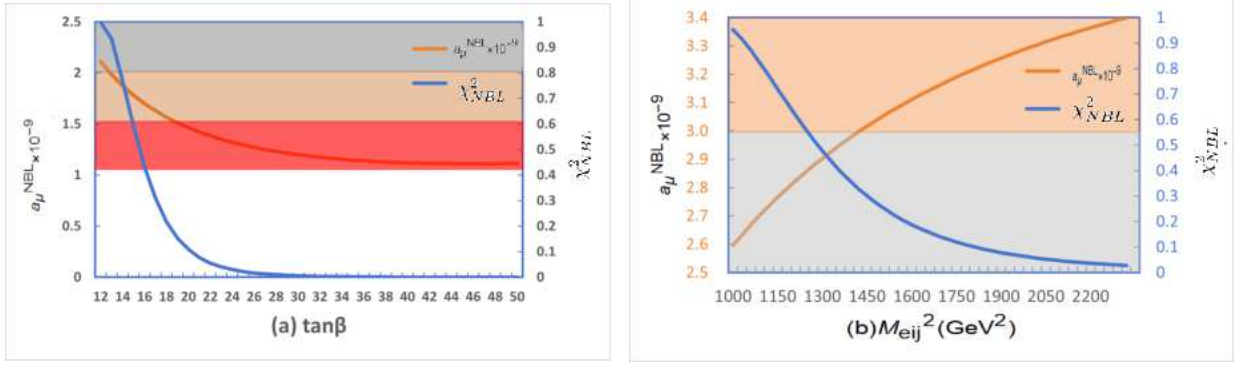


FIG. 5:  $a_\mu^{NBL}$  and  $\chi_{NBL}^2$  in  $\tan \beta$  plane (a) and  $M_{eij}^2$  plane (b).

We use the parameters as  $M_{BB'} = 0.1 \text{ TeV}$ ,  $M_e^2 = 1.5 \text{ TeV}^2$ ,  $M_L^2 = 0.16 \text{ TeV}^2$ ,  $T_{eii} = 3 \text{ TeV}$  and  $T_{eij} = 0$  in Fig.5. Next, we plot  $\tan \beta$  versus  $a_\mu^{NBL}$  and  $\chi_{NBL}^2$  in the Fig. 5(a). The light red area in the figure represents the  $3\sigma$  range. The two lines are all decreasing functions as  $\tan \beta$  turns large in the range of  $12 < \tan \beta < 50$ . The downward trend of  $a_\mu^{NBL}$  is relatively gentle, and when  $\tan \beta$  is greater than 20,  $a_\mu^{NBL}$  is all within the range of  $3\sigma$ . The downward trend of  $\chi_{NBL}^2$  is relatively severe.  $\tan \beta$  must be a sensitive parameter because it appears almost in all mass matrices of fermions, scalars, and Majoranas, and it can affect the vertex couplings and masses of particles by directly affecting  $v_d$  and  $v_u$ . By influencing these factors,  $\tan \beta$  shows a downward trend.

Finally, we plot  $M_{eij}^2$  versus  $a_\mu^{NBL}$  and  $\chi_{NBL}^2$  in the Fig.5(b). In the figure,  $a_\mu^{NBL}$  increases with the increase of  $M_{eij}^2$ , while  $\chi_{NBL}^2$  decreases with the increase of  $M_{eij}^2$ . The decrease in  $\chi_{NBL}^2$  is because the growth of  $a_\mu^{NBL}$  exceeds the range of  $1\sigma$ , so it is reasonable for the two curves to have different trends. When  $M_{eij}^2$  is greater than  $1000 \text{ GeV}^2$ , it enters the  $1\sigma$  range, and when  $M_{eij}^2$  is greater than  $1450 \text{ GeV}^2$ , it enters the  $2\sigma$  range.  $M_{eij}^2$  is the flavor mixing parameters appearing in the mass matrices of the slepton. The increase of  $M_{eij}^2$  affects the contributions of the slepton, thereby causing  $a_\mu^{NBL}$  to increase with the increase of  $M_{eij}^2$ .

## B. The multi-dimensional scatter plots

In this section of the work, we select six parameters  $\tan\beta$ ,  $T_e$ ,  $M_L^2$ ,  $M_{eij}^2$ ,  $T_{eij}$  and  $M_e^2$  discussed in the one-dimensional graph to draw the scatter plots.

TABLE II: The meaning of shape style in Fig. 6 and Fig. 7

Shape style	Fig. 6 and Fig. 7
▲	$0 < a_\mu^{NBL} < 2.01 \times 10^{-9}$
■	$2.01 \times 10^{-9} \leq a_\mu^{NBL} < 2.97 \times 10^{-9}$
●	$2.97 \times 10^{-9} \leq a_\mu^{NBL}$

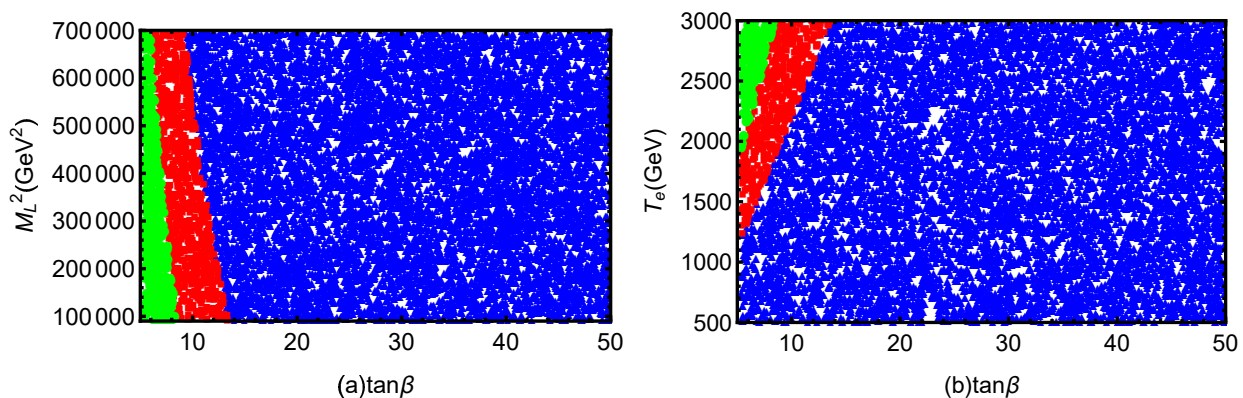


FIG. 6:  $a_\mu^{NBL}$  in  $\tan\beta - M_L^2$  plane(a),  $\tan\beta - T_e$  plane(b).

Supposing  $T_e = 3 \text{ TeV}$ ,  $M_e^2 = 1.5 \text{ TeV}^2$ ,  $T_{eij} = 0$ ,  $M_{eij}^2 = 0$ , we plot  $a_\mu^{NBL}$  in the  $\tan\beta$  versus  $M_L^2$  in the Fig.6(a). Within the range of  $5 < \tan\beta < 50$  and  $0.1 \text{ TeV}^2 < M_L^2 < 0.7 \text{ TeV}^2$ , the ● and ■ are slightly tilted and distributed on the left side of the graph. When  $5 < \tan\beta < 7$ , the proportion of ● is higher. When  $7 < \tan\beta < 13$ , the proportion of ■ is higher. When  $13 < \tan\beta < 50$ , there are only ▲. We can conclude that  $a_\mu^{NBL}$  decreases with the increase of  $\tan\beta$ , and the trend is more intense.  $a_\mu^{NBL}$  also decreases with the increase of  $M_L^2$ , but the trend is relatively gentle. This is consistent with the decreasing trend of  $a_\mu^{NBL}$  as  $\tan\beta$  and  $M_L^2$ , which are shown in Fig.3(b) and Fig.5(a). And the reduction amplitude is also consistent with the one-dimensional graph.

With  $M_L^2 = 0.16 \text{ TeV}^2$ ,  $M_e^2 = 1.5 \text{ TeV}^2$ ,  $T_{eij} = 0$ ,  $M_{eij}^2 = 0$ , Fig.6(b) displays a plot of  $a_\mu^{NBL}$  in the  $\tan\beta$  versus  $T_e$  plane. We can clearly see that the space is roughly divided into

three parts. The  $\bullet$  present a triangular shape distributed in the upper left, the  $\blacksquare$  present a strip close to the green points, and the rest are filled with  $\blacktriangle$ . Both  $\tan\beta$  and  $T_e$  are sensitive parameters, and  $a_\mu^{NBL}$  decreases with the increase of  $\tan\beta$  and increases with the increase of  $T_e$ , which is consistent with the feature of one-dimensional graph.

In Fig.6, we all select  $\tan\beta$  as the horizontal axis. It can be seen intuitively that  $\tan\beta$  has a strong influence on  $a_\mu^{NBL}$ . The vertical axis of Fig.6(a) is  $M_L^2$ , and the vertical axis of Fig.6(b) is  $T_e$ . One shows an increasing trend and the other shows a decreasing trend. We can conclude that all three are sensitive parameters. When  $7 < \tan\beta < 13$ ,  $0.1 \text{ TeV}^2 < M_L^2 < 0.7 \text{ TeV}^2$ ,  $1.5 \text{ TeV} < T_e < 3 \text{ TeV}$ , the value of  $a_\mu^{NBL}$  is closest to the range of  $1\sigma$ .

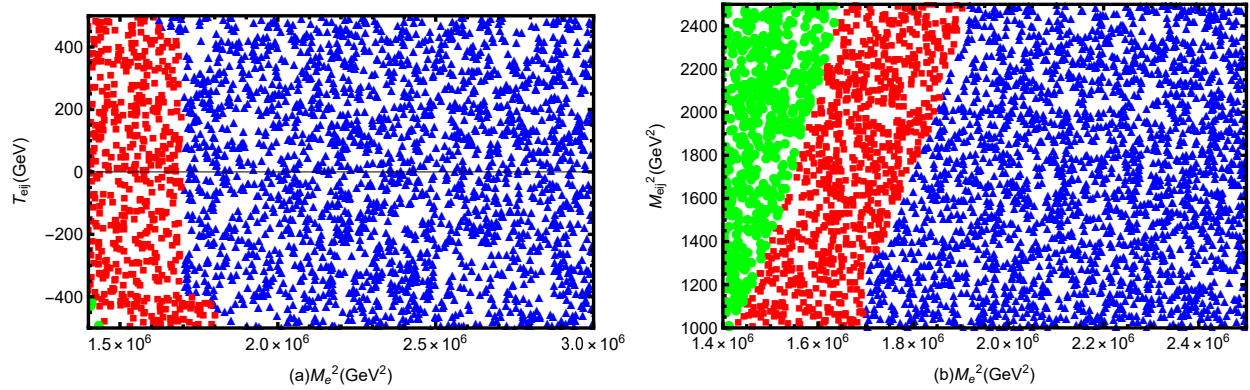


FIG. 7:  $a_\mu^{NBL}$  in  $M_e^2 - T_{eij}$  plane(a),  $M_e^2 - M_{eij}^2$  plane(b).

We suppose the parameters with  $T_e = 3 \text{ TeV}$ ,  $\tan\beta = 10$ ,  $M_L^2 = 0.16 \text{ TeV}^2$ ,  $M_{eij}^2 = 0$  in Fig. 7(a), and display a plot of  $a_\mu^{NBL}$  in the  $M_e^2$  versus  $T_{eij}$  plane. The  $\bullet$  is only scattered in the lower left corner,  $\blacksquare$  is in the range of  $1.5 \text{ TeV}^2 < M_e^2 < 1.75 \text{ TeV}^2$ ,  $\blacktriangle$  is in the range of  $1.75 \text{ TeV}^2 < M_e^2 < 3 \text{ TeV}^2$ .  $M_e^2$  is an important parameter affecting  $a_\mu^{NBL}$ , and the effect of  $T_{eij}$  is relatively weak.

With  $T_e = 3 \text{ TeV}$ ,  $\tan\beta = 10$ ,  $T_{eij} = 0$ ,  $M_L^2 = 0.16 \text{ TeV}^2$ , we plot  $a_\mu^{NBL}$  in the  $M_e^2$  versus  $M_{eij}^2$  plane in the Fig.7(b). The three parts of the figure show a tilted pattern, and the points of the three colors exist in the full range of  $M_{eij}^2$ , indicating that  $M_{eij}^2$  has an effect on  $a_\mu^{NBL}$ , and  $a_\mu^{NBL}$  increases with the increase of  $M_{eij}^2$ . The  $\blacksquare$  is basically distributed in the range of  $1.4 \text{ TeV}^2 < M_e^2 < 1.7 \text{ TeV}^2$ , showing a parallelogram form, which satisfies the  $1\sigma$  limit. Much space is filled with the  $\blacktriangle$ , which are located in the right part.

## V. CONCLUSION

In this paper, we use the effective Lagrangian method to research the one-loop diagrams and some important two-loop diagrams. The studied contributions are composed of one-loop diagrams, the two-loop Barr-Zee type diagrams with fermion sub-loop, the two-loop rainbow type diagrams with fermion sub-loop and the vector bosons( $\gamma$ ,  $Z$ ,  $W$ ), the diamond type diagrams in Refs.[41, 42] possessing large factors

$$a_\mu = a_\mu^{1L} + a_\mu^{2L, BZ} + a_\mu^{2L, RB} + a_\mu^{2L, DIA}. \quad (26)$$

We consider the latest experimental constraints and adjust the sensitive parameters. In the end, we obtain rich numerical results and interesting one-dimensional and multi-dimensional scatter plots.

In the one-dimensional graph, we select  $\tan\beta$ ,  $T_e$ ,  $M_L^2$ ,  $M_e^2$ ,  $M_{BB'}$  and  $M_{eij}^2$  to study muon MDM. Through the trend of the two lines, we can conclude that these parameters play an important role in  $a_\mu^{NBL}$ , where  $M_e^2$  and  $T_e$  have a strong influence on  $a_\mu^{NBL}$ . In the scatter plot, we select six parameters  $\tan\beta$ ,  $T_e$ ,  $M_L^2$ ,  $M_e^2$ ,  $M_{BB'}$  and  $T_{eij}$ . The characteristics of scatter plot is consistent with the one-dimensional diagram, indicating that  $M_e^2$  and  $\tan\beta$  have a strong influence on  $a_\mu^{NBL}$ . Other parameters also have a significant impact, but not as strong as the influence of  $M_e^2$  and  $\tan\beta$  on  $a_\mu^{NBL}$ . From the data obtained in the figure, most numerical results of  $a_\mu^{NBL}$  are in  $2\sigma$ , which can compensate the departure between the experiment data and the SM prediction. Utilizing the parameter space that we have derived to guide experimental design can help optimize experimental conditions and increase the likelihood of discovering SUSY particles. After collecting experimental data, we search for data that is consistent with theoretical predictions. By comparing the experimental data with theoretical predictions, we can further refine the parameter space, thereby enhancing the possibility of detecting SUSY particles.

It is well known that there are many two-loop diagrams that contribute to muon MDM. Some two-loop diagrams that have not been studied can also give important corrections to muon MDM, which can further improve the theoretical value. Since the calculation of two-loop diagrams are very complicated, we will study other two-loop diagrams in future work.

## Acknowledgments

This work is supported by National Natural Science Foundation of China (NNSFC) (No.12075074), Natural Science Foundation of Hebei Province (A2023201040, A2022201022, A2022201017, A2023201041), Natural Science Foundation of Hebei Education Department (QN2022173), Post-graduate's Innovation Fund Project of Hebei University (HBU2024SS042), the youth top-notch talent support program of the Hebei Province.

## Appendix A: Mass matrix and coupling in N-B-LSSM

The mass matrix for chargino is:

$$m_{\chi^-} = \begin{pmatrix} M_2 & \frac{1}{\sqrt{2}}g_2v_\mu \\ \frac{1}{\sqrt{2}}g_2v_d & \frac{1}{\sqrt{2}}\lambda v_S \end{pmatrix}. \quad (\text{A1})$$

This matrix is diagonalized by U and V:

$$U^* m_{\chi^-} V^\dagger = m_{\chi^-}^{dia}. \quad (\text{A2})$$

The mass matrix for neutrino is:

$$m_\nu = \begin{pmatrix} 0 & \frac{1}{\sqrt{2}}v_u Y_\nu^T \\ \frac{1}{\sqrt{2}}v_u Y_\nu & \sqrt{2}v_\eta Y_\chi \end{pmatrix}. \quad (\text{A3})$$

This matrix is diagonalized by  $U^V$ :

$$U^{V,*} m_\nu U^{V,\dagger} = m_\nu^{dia}. \quad (\text{A4})$$

$$m_{A^0}^2 = \begin{pmatrix} m_{\sigma_d\sigma_d} & m_{\sigma_u\sigma_d} & m_{\sigma_1\sigma_d} & m_{\sigma_2\sigma_d} & m_{\sigma_s\sigma_d} \\ m_{\sigma_d\sigma_u} & m_{\sigma_u\sigma_u} & m_{\sigma_1\sigma_u} & m_{\sigma_2\sigma_u} & m_{\sigma_s\sigma_u} \\ m_{\sigma_d\sigma_1} & m_{\sigma_u\sigma_1} & m_{\sigma_1\sigma_1} & m_{\sigma_2\sigma_1} & m_{\sigma_s\sigma_1} \\ m_{\sigma_d\sigma_2} & m_{\sigma_u\sigma_2} & m_{\sigma_1\sigma_2} & m_{\sigma_2\sigma_2} & m_{\sigma_s\sigma_2} \\ m_{\sigma_d\sigma_s} & m_{\sigma_u\sigma_s} & m_{\sigma_1\sigma_s} & m_{\sigma_2\sigma_s} & m_{\sigma_s\sigma_s} \end{pmatrix}. \quad (\text{A5})$$

Eq.(A5) is the CP-odd Higgs mass squared matrix, whose elements are

$$m_{\sigma_d\sigma_d} = m_{H_d}^2 + \frac{1}{8} \left( (g_1^2 + g_2^2 + g_{YB}^2)(v_d^2 - v_u^2) + 2g_{YB}g_B(v_\eta^2 - v_{\bar{\eta}}^2) \right) + \frac{1}{2}(v_u^2 + v_S^2)|\lambda|^2,$$

$$\begin{aligned}
m_{\sigma_d\sigma_u} &= \frac{1}{\sqrt{2}}v_S T_\lambda + \left(\frac{1}{2}\kappa v_S^2 - \frac{1}{2}\lambda_2 v_\eta v_{\bar{\eta}}\right)\lambda, \\
m_{\sigma_u\sigma_u} &= m_{H_u}^2 + \frac{1}{8}\left((g_1^2 + g_{YB}^2 + g_2^2)(v_u^2 - v_d^2) + 2g_{YB}g_B(v_\eta^2 - v_{\bar{\eta}}^2)\right) + \frac{1}{2}(v_d^2 + v_S^2)|\lambda|^2, \\
m_{\sigma_1\sigma_1} &= m_\eta^2 + \frac{1}{4}\left(g_{YB}g_B(v_d^2 - v_u^2) + 2g_B^2(v_\eta^2 - v_{\bar{\eta}}^2)\right) + \frac{1}{2}(v_\eta^2 + v_S^2)|\lambda_2|^2, \\
m_{\sigma_1\sigma_2} &= \frac{1}{2}\left(-v_d v_u \lambda \lambda_2 + v_S(\sqrt{2}T_2 + v_S \lambda_2 \kappa)\right), \\
m_{\sigma_2\sigma_2} &= m_{\bar{\eta}}^2 + \frac{1}{4}\left(g_{YB}g_B(v_u^2 - v_d^2) - 2g_B^2(v_\eta^2 - v_{\bar{\eta}}^2)\right) + \frac{1}{2}(v_\eta^2 + v_S^2)|\lambda_2|^2, \\
m_{\sigma_d\sigma_s} &= -v_u\left(v_S\kappa\lambda - \frac{1}{\sqrt{2}}T_\lambda\right), & m_{\sigma_d\sigma_1} &= \frac{1}{2}v_u v_{\bar{\eta}}\lambda_2\lambda, \\
m_{\sigma_u\sigma_s} &= -v_d\left(v_S\kappa\lambda - \frac{1}{\sqrt{2}}T_\lambda\right), & m_{\sigma_u\sigma_1} &= \frac{1}{2}v_d v_{\bar{\eta}}\lambda_2\lambda, \\
m_{\sigma_1\sigma_s} &= -v_{\bar{\eta}}\left(v_S\kappa\lambda_2 - \frac{1}{\sqrt{2}}T_2\right), & m_{\sigma_d\sigma_2} &= \frac{1}{2}v_u v_\eta\lambda_2\lambda, \\
m_{\sigma_2\sigma_s} &= -v_\eta\left(v_S\kappa\lambda_2 - \frac{1}{\sqrt{2}}T_2\right), & m_{\sigma_u\sigma_2} &= \frac{1}{2}v_d v_\eta\lambda_2\lambda, \\
m_{\sigma_s\sigma_s} &= m_S^2 + (\kappa v_S^2 + \lambda_2 v_\eta v_{\bar{\eta}} + \lambda v_d v_u)\kappa + \frac{1}{2}|\lambda|^2(v_d^2 + v_u^2) + \frac{1}{2}|\lambda_2|^2(v_\eta^2 + v_{\bar{\eta}}^2) \\
&\quad - \sqrt{2}v_S T_\kappa.
\end{aligned} \tag{A6}$$

The used vertexes in Eq.(12) are:

$$\begin{aligned}
A_R &= \frac{1}{\sqrt{2}}Z_{k2}^E(g_1 N_{j1}^* + g_2 N_{j2}^* + g_{YB} N_{j5}^*) - N_{j3}^* Y_\mu Z_{k5}^E, \\
A_L &= -\frac{1}{\sqrt{2}}Z_{k5}^E[2g_1 N_{j1} + (2g_{YB} + g_B)N_{j5}] - Y_\mu^* Z_{k2}^E N_{j3}, \\
B_L &= -\frac{1}{\sqrt{2}}U_{i2}^* Z_{k2}^{I*} Y_\mu, & B_R &= \frac{1}{\sqrt{2}}g_2 Z_{k2}^{I*} V_{i1}, \\
C_L &= \frac{1}{\sqrt{2}}U_{i2}^* Z_{k2}^{R*} Y_\mu, & C_R &= -\frac{1}{\sqrt{2}}g_2 Z_{k2}^{R*} V_{i1}.
\end{aligned} \tag{A7}$$

$$M_\nu = \begin{pmatrix} 0 & \frac{v_u}{\sqrt{2}}(Y_\nu^T)^{IJ} \\ \frac{v_u}{\sqrt{2}}(Y_\nu)^{IJ} & \sqrt{2}v_{\bar{\eta}}(Y_\chi)^{IJ} \end{pmatrix}, \quad \text{with } I, J = 1, 2, 3. \tag{A8}$$

The effective light neutrino mass matrix is in general given as  $m_{eff} = -mM^{-1}m^T$ , with

$$m = \frac{1}{\sqrt{2}}v_u Y_\nu^T, \quad M = \sqrt{2}v_{\bar{\eta}} Y_\chi, \tag{A9}$$

For the effective neutrino mass matrix  $m_{eff}$ , we obtain the Hermitian matrix

$$\mathcal{H} = m_{eff}^\dagger m_{eff}. \tag{A10}$$

We define some notations to express the formula succinctly.

$$\begin{aligned}
a &= \text{Tr}(\mathcal{H}), \\
b &= \mathcal{H}_{11}\mathcal{H}_{22} + \mathcal{H}_{11}\mathcal{H}_{33} + \mathcal{H}_{22}\mathcal{H}_{33} - \mathcal{H}_{12}^2 - \mathcal{H}_{13}^2 - \mathcal{H}_{23}^2, \\
c &= \text{Det}(\mathcal{H}), \\
p &= \sqrt{a^2 - 3b}, \\
\phi &= \frac{1}{3} \arccos\left(\frac{1}{p^3}\left(a^3 - \frac{9}{2}ab + \frac{27}{2}c\right)\right).
\end{aligned} \tag{A11}$$

Thus we obtain the eigenvalues of the  $3 \times 3$  matrix  $\mathcal{H}$

$$\begin{aligned}
m_1^2 &= \frac{a}{3} - \frac{1}{3}p(\cos \phi + \sqrt{3} \sin \phi), \\
m_2^2 &= \frac{a}{3} - \frac{1}{3}p(\cos \phi - \sqrt{3} \sin \phi), \\
m_3^2 &= \frac{a}{3} + \frac{2}{3}p \cos \phi.
\end{aligned} \tag{A12}$$

The normalized eigenvectors for the mass squared matrix  $\mathcal{H}$  are given as

$$\begin{aligned}
\begin{pmatrix} (U_\nu)_{11} \\ (U_\nu)_{21} \\ (U_\nu)_{31} \end{pmatrix} &= \frac{1}{\sqrt{|X_1|^2 + |Y_1|^2 + |Z_1|^2}} \begin{pmatrix} X_1 \\ Y_1 \\ Z_1 \end{pmatrix}, \\
\begin{pmatrix} (U_\nu)_{12} \\ (U_\nu)_{22} \\ (U_\nu)_{32} \end{pmatrix} &= \frac{1}{\sqrt{|X_2|^2 + |Y_2|^2 + |Z_2|^2}} \begin{pmatrix} X_2 \\ Y_2 \\ Z_2 \end{pmatrix}, \\
\begin{pmatrix} (U_\nu)_{13} \\ (U_\nu)_{23} \\ (U_\nu)_{33} \end{pmatrix} &= \frac{1}{\sqrt{|X_3|^2 + |Y_3|^2 + |Z_3|^2}} \begin{pmatrix} X_3 \\ Y_3 \\ Z_3 \end{pmatrix},
\end{aligned} \tag{A13}$$

with

$$\begin{aligned}
X_1 &= (\mathcal{H}_{22} - m_{\nu 1}^2)(\mathcal{H}_{33} - m_{\nu 1}^2) - \mathcal{H}_{23}^2, \\
Y_1 &= \mathcal{H}_{13}\mathcal{H}_{23} - \mathcal{H}_{12}(\mathcal{H}_{33} - m_{\nu 1}^2), \\
Z_1 &= \mathcal{H}_{12}\mathcal{H}_{23} - \mathcal{H}_{13}(\mathcal{H}_{22} - m_{\nu 1}^2), \\
X_2 &= \mathcal{H}_{13}\mathcal{H}_{23} - \mathcal{H}_{12}(\mathcal{H}_{33} - m_{\nu 2}^2), \\
Y_2 &= (\mathcal{H}_{11} - m_{\nu 2}^2)(\mathcal{H}_{33} - m_{\nu 2}^2) - \mathcal{H}_{13}^2,
\end{aligned}$$

$$\begin{aligned}
Z_2 &= \mathcal{H}_{12}\mathcal{H}_{13} - \mathcal{H}_{23}(\mathcal{H}_{11} - m_{\nu 2}^2), \\
X_3 &= \mathcal{H}_{12}\mathcal{H}_{23} - \mathcal{H}_{13}(\mathcal{H}_{22} - m_{\nu 3}^2), \\
Y_3 &= \mathcal{H}_{12}\mathcal{H}_{13} - \mathcal{H}_{23}(\mathcal{H}_{11} - m_{\nu 3}^2), \\
Z_3 &= (\mathcal{H}_{11} - m_{\nu 3}^2)(\mathcal{H}_{22} - m_{\nu 3}^2) - \mathcal{H}_{12}^2.
\end{aligned} \tag{A14}$$

In a general way, we define the mixing angles among three tiny neutrinos as

$$\begin{aligned}
\sin \theta_{13} &= |(U_\nu)_{13}|, & \cos \theta_{13} &= \sqrt{1 - |(U_\nu)_{13}|^2}, \\
\sin \theta_{23} &= \frac{|(U_\nu)_{23}|}{\sqrt{1 - |(U_\nu)_{13}|^2}}, & \cos \theta_{23} &= \frac{|(U_\nu)_{33}|}{\sqrt{1 - |(U_\nu)_{13}|^2}}, \\
\sin \theta_{12} &= \frac{|(U_\nu)_{12}|}{\sqrt{1 - |(U_\nu)_{13}|^2}}, & \cos \theta_{12} &= \frac{|(U_\nu)_{11}|}{\sqrt{1 - |(U_\nu)_{13}|^2}}.
\end{aligned} \tag{A15}$$

- 
- [1] S.L. Glashow, H. Georgi, *Phys. Rev. Lett.* **32** (1974) 438-441.
  - [2] S. Weinberg, *Phys. Rev. Lett.* **19** (1967) 1264-1266.
  - [3] S. Weinberg, *Phys. Rev. D* **19** (1979) 1277-1280.
  - [4] A. Salam, J. C. Ward, *Phys. Rev. Lett.* **30** (1973) 1268-1271.
  - [5] H.P. Nilles, *Phys. Rept.* **110** (1984) 1-162.
  - [6] H.E. Haber, G.L. Kane, *Phys. Rept.* **117** (1985) 75-263.
  - [7] Rosiek, *Phys. Rev. D* **41** (1990) 3464.
  - [8] T. Aoyama, N. Asmussen, M. Benayoun, et al., *Phys. Rept.* **887** (2020) 1.
  - [9] G.W. Bennett, et al., *Phys. Rev. D* **73** (2006) 072003.
  - [10] A. Keshavarzi, D. Nomura, T. Teubner, *Phys. Rev. D* **97** (2018) 114025.
  - [11] G. Colangelo, M. Hoferichter, P. Stoffer, *J. High Energy Phys.* **02** (2019) 006.
  - [12] M. Hoferichter, B.L. Hoid, B. Kubis, *J. High Energy Phys.* **08** (2019) 137.
  - [13] M. Davier, A. Hoecker, B. Malaescu, et al., *Eur. Phys. J. C* **80** (2020) 241.
  - [14] A. Keshavarzi, D. Nomura, T. Teubner, *Phys. Rev. D* **101** (2020) 014029.
  - [15] T. Blum, P.A. Boyle, V. Gulpers, et al., *Phys. Rev. Lett.* **121** (2018) 022003.
  - [16] T. Aoyama, M. Hayakawa, T. Kinoshita, et al., *Phys. Rev. Lett.* **109** (2012) 111808.
  - [17] G. Colangelo, F. Hagelstein, M. Hoferichter, et al., *J. High Energy Phys.* **03** (2020) 101.
  - [18] G. Eichmann, C.S. Fischer, R. Williams, *Phys. Rev. D* **101** (2020) 054015.

- [19] T. Blum, N. Christ, M. Hayakawa, et al., *Phys. Rev. Lett.* **124** (2020) 132002.
- [20] T. Aoyama, T. Kinoshita, M. Nio, *Atoms.* **7** (2019) 28.
- [21] A. Czarnecki, W.J. Marciano, A. Vainshtein, *Phys. Rev. D* **67** (2003) 073006.
- [22] C. Gnendiger, D. Stockinger, H.S. Kim, *Phys. Rev. D* **88** (2013) 053005.
- [23] M.T. Hansen, A. Patella, *J. High Energy Phys.* **10** (2020) 029.
- [24] D.P. Aguillard, et al. *Phys. Rev. Lett.* **131** (2023) 161802.
- [25] A. Datta, D. Marfatia, L. Mukherjee, *Phys. Rev. D* **109** (2024) L031701.
- [26] X. Wang, X.X. Long, Y.T. Wang, et al., *J. Phys. G* **51** (2024) 015004.
- [27] G. Degrossi, G. Giudice, *Phys. Rev. D* **58** (1998) 053007.
- [28] T.F. Feng, L. Sun, X.Y. Yang, *Phys. Rev. D* **77** (2008) 116008.
- [29] T.F. Feng, X.Y. Yang, *Nucl. Phys. B* **814** (2009) 101.
- [30] S.M. Zhao, T.F. Feng, H.B. Zhang, et al., *J. High Energy Phys.* **11** (2014) 119.
- [31] J.L. Yang, T.F. Feng, Y.L. Yan, et al., *Phys. Rev. D* **99** (2019) 015002.
- [32] G. Belanger, J.D. Silva, H.M. Tran, *Phys. Rev. D* **95** (2017) 115017.
- [33] V. Barger, P.F. Perez, S. Spinner, *Phys. Rev. Lett.* **102** (2009) 181802.
- [34] P.H. Chankowski, S. Pokorski, J. Wagner, *Eur. Phys. J. C* **47** (2006) 187.
- [35] J.L. Yang, T.F. Feng, S.M. Zhao, et al., *Eur. Phys. J. C* **78** (2018) 714.
- [36] S.M. Zhao, L.H. Su, X.X. Dong, et al., *J. High Energy Phys.* **03** (2022), 101.
- [37] G. Cacciapaglia, C. Csáki, G. Marandella, et al., *Phys. Rev. D* **74** (2006) 033011.
- [38] ATLAS collaboration, *Phys. Lett. B* **796** (2019) 68.
- [39] X.Y. Yang, T.F. Feng, *Phys. Lett. B* **675** (2009) 43.
- [40] T.F. Feng, L. Sun, X.Y. Yang, *Nucl. Phys. B* **800** (2008) 221-252.
- [41] S.M. Zhao, T.F. Feng, T. Li, et al., *MPLA* **27** (2012) 1250045.
- [42] S.M. Zhao, X.X. Dong, L.H. Su, et al., *Eur. Phys. J. C* **80** (2020) 823.
- [43] L. Basso, *Adv. High Energy Phys.* **2015** (2015) 980687.
- [44] R.L. Workman, et al., *Prog. Theor. Exp. Phys.* **2022** (2022) 083C01.
- [45] H. Bahl, T. Biekötter, S. Heinemeyer, et al., *Comput. Phys. Commun.* **291** (2023) 108803.